

Suppressing the Shuttle Effect and Dendrite Growth in Lithium-Sulfur Batteries

Jianan Wang, Shanshan Yi, Jianwei Liu, Sun Shiyi, Yunpeng Liu, Duowen Yang, Kai Xi, Guoxin Gao, Amr Abdelkader, Wei Yan, Shujiang Ding, and Ramachandran Vasant Kumar

ACS Nano, **Just Accepted Manuscript** • DOI: 10.1021/acsnano.0c02241 • Publication Date (Web): 07 Jul 2020

Downloaded from pubs.acs.org on July 7, 2020

Just Accepted

“Just Accepted” manuscripts have been peer-reviewed and accepted for publication. They are posted online prior to technical editing, formatting for publication and author proofing. The American Chemical Society provides “Just Accepted” as a service to the research community to expedite the dissemination of scientific material as soon as possible after acceptance. “Just Accepted” manuscripts appear in full in PDF format accompanied by an HTML abstract. “Just Accepted” manuscripts have been fully peer reviewed, but should not be considered the official version of record. They are citable by the Digital Object Identifier (DOI®). “Just Accepted” is an optional service offered to authors. Therefore, the “Just Accepted” Web site may not include all articles that will be published in the journal. After a manuscript is technically edited and formatted, it will be removed from the “Just Accepted” Web site and published as an ASAP article. Note that technical editing may introduce minor changes to the manuscript text and/or graphics which could affect content, and all legal disclaimers and ethical guidelines that apply to the journal pertain. ACS cannot be held responsible for errors or consequences arising from the use of information contained in these “Just Accepted” manuscripts.

Suppressing the Shuttle Effect and Dendrite Growth in Lithium-Sulfur Batteries

Jianan Wang,^{†,§} Shanshan Yi,[†] Jianwei Liu,[†] Shiyi Sun,[†] Yunpeng Liu,[†] Duowen Yang,[†] Kai Xi,^{*,‡,¶} Guoxin Gao,^{†,§} Amr Abdelkader,[‡] Wei Yan,^{*,†,§} Shujiang Ding,^{*,†,§} and Ramachandran Vasant Kumar[¶]

[†]Department of Environmental Science and Engineering, Department of Applied Chemistry, School of Chemistry, MOE Key Laboratory for Nonequilibrium Synthesis and Modulation of Condensed Matter, State Key Laboratory for Electrical Insulation and Power Equipment, Xi'an Jiaotong University, Xi'an 710049, China.

[‡]Department of Engineering, University of Cambridge, Cambridge, CB3 0FA, United Kingdom.

[¶]Department of Materials Science and Metallurgy, University of Cambridge, Cambridge, CB3 0FS, United Kingdom.

[‡]Faculty of Science and Technology, Bournemouth University, Talbot Campus, Fern Barrow, Poole, BH12 5BB, United Kingdom.

[§]Xi'an Jiaotong University & Shaanxi Quantong Joint Research Institute of New Energy Vehicles Power

*E-mail: dingsj@xjtu.edu.cn (S. Ding); yanwei@xjtu.edu.cn (W. Yan); kx210@cam.ac.uk (K. Xi)

1
2
3
4 **ABSTRACT:** Practical applications of lithium-sulfur batteries are simultaneously hindered by
5
6 two serious problems occurring separately in both electrodes, namely, the shuttle effects of
7
8 lithium polysulfides and the uncontrollable growth of lithium dendrites. Herein, to explore a
9
10 facile integrated approach to tackle both problems as well as guarantee the efficient charge
11
12 transfer, we used two-dimension hexagonal VS₂ flakes as the building blocks to assemble
13
14 nanotowers on the separators, forming symmetrical double-side-modified polypropylene
15
16 separator without blocking the membrane pores. Benefiting from the “sulfiphilic” and
17
18 “lithiophilic” properties, high interfacial electronic conductivity and unique hexagonal tower-
19
20 form nanostructure, the D-HVS@PP separator not only guarantee the effective suppression of
21
22 lithium polysulfide shuttle and the rapid ion/electron transfer, but also realize the uniform and
23
24 stable lithium nucleation and growth during cycling. Hence, just at the expense of an 11%
25
26 increase in the separator weight (0.14 mg cm⁻²), D-HVS@PP separator delivers an over 16 times
27
28 higher initial areal capacity (8.3 mAh cm⁻²) than conventional PP separator (0.5 mAh cm⁻²) under
29
30 high sulfur-loading condition (9.24 mg cm⁻²). Even when used under a low electrolyte/sulfur
31
32 ratio of 4 mL g⁻¹ and a practically relevant N/P ratio of 1.7, D-HVS@PP separator still enabled
33
34 stable cycling with a high cell-level gravimetric energy density. The potentials in broader
35
36 applications (Li-S pouch battery and Li-LiFePO₄ battery) and the promising commercial
37
38 prospect (large-scale production and recyclability) of the developed separator are also
39
40 demonstrated.
41
42
43
44
45
46
47
48
49

50 **KEYWORDS:** *lithium-sulfur batteries, amphiphilic, separator, lithium dendrites, recyclable,*
51
52 *shuttle effect*
53
54
55
56
57
58
59
60

1
2
3 The rapid development of portable electronic devices, electric vehicles and smart grids
4 has evoked the ever-increasing demand for high-energy-density energy storage systems
5 with sustainable electrochemical performances.¹⁻³ Lithium-sulfur (Li-S) batteries are
6 regarded as a potential alternative to current state-of-the-art Li-ion batteries owing to their
7 high theoretical capacity (1675 mAh g⁻¹ of sulfur) and energy density (2600 Wh kg⁻¹),
8 low cost and environmental friendliness.⁴⁻⁶ Despite such a bright perspective, the practical
9 implementation of Li-S batteries is still facing some tough challenges. In terms of the
10 sulfur cathode, the severe “shuttling effect” of the dissolved intermediate lithium
11 polysulfides (Li₂S_x) gives rise to low active sulfur utilization, low coulombic efficiency
12 and rapid capacity decay;⁷⁻⁹ For the lithium anode, the uncontrollable growth of lithium
13 “dendrites” on the surface of lithium metal induces a series of adverse effects, such as the
14 evolution of “dead” lithium, unstable solid electrolyte interphase (SEI), increased
15 polarization and even explosion hazards.^{10, 11} Due to the disparate reaction mechanism
16 and different physicochemical characteristics of the sulfur cathode and the lithium anode,
17 synchronously suppressing the shuttle effect and the dendrite growth during long-term
18 cycling has become a formidable technical challenge for the practical application of Li-S
19 batteries.

20
21
22 To date, several approaches have been developed to address these issues, including
23 designing cathode host materials,^{12, 13} inserting interlayer,¹⁴ substituting binders¹⁵ and
24 modifying the separator or the lithium anode.¹⁶⁻¹⁹ The majority of these technical
25 strategies only focus on one part of the cell. Adopting an integrated approach that can
26 simultaneously solve the lithium dendrites and Li₂S_x shuttle effect maybe the way
27 forward to make Li-S batteries achieve the commercial realization. Separators, as the

1
2
3 essential medium directly contacting and interacting with both the anode and the cathode,
4 play a vital role in the battery system.²⁰⁻²³ Functionalizing both sides of commercially
5 available separators is considered to be a facile/effective strategy in controlling the
6 interfacial reactions of both the multielectron conversion of sulfur/polysulfide and the
7 lithium deposition/dissolution, further boosting the overall battery performance.²⁴⁻²⁶ For
8 this purpose, some asymmetric separator structures have been developed recently to
9 satisfy the distinct requirements of both the cathode and the anode sides.^{20, 27, 28} However,
10 the majority of these separators has shown difficulties to maintain the inherent pore
11 structures of the separator itself during the charging/discharging process, representing a
12 constraint for the high-flux Li^+ diffusion.^{20, 29} In addition, the complicated design of the
13 asymmetrical separator inevitably increases the difficulty for the separator
14 commercialization. Based on the above analysis, it would be appealing to rationally select
15 and design a multifunctional material using for separator modification, which could
16 simultaneously meet distinct demands of the anode and cathode in Li-S batteries as well
17 as guarantee the smooth ion diffusion.
18
19
20
21
22
23
24
25
26
27
28
29
30
31
32
33
34
35
36

37 Vanadium disulfide (VS_2) is one of the transition-metal dichalcogenides (TMDs) that
38 has attracted increasing interests in the fields of electrochemical energy storage in recent
39 years because of its unique chemical/physical characteristics, intrinsic metallic behavior
40 and two-dimensional (2D) layered structure.³⁰⁻³² Cui *et al.*³⁰ have reported that
41 commercial VS_2 could exhibit higher capacity and better cycling stability compared with
42 other TMDs materials (TiS_2 , CoS_2 , Ni_3S_2 , SnS_2 and FeS) and graphite when used as the
43 cathode host material in Li-S batteries. They attributed the performance enhancement to
44 the high conductivity, strong interaction with Li_2S_x , easy Li-ion transport and excellent
45
46
47
48
49
50
51
52
53
54
55
56
57
58
59
60

1
2
3 catalyzing reduction/oxidation capability of VS_2 . All these superiorities signify that VS_2
4
5 deserves specific attention as a promising functional material not only for the cathode but
6
7 also as a modifier for the separator, an area which hardly been investigated in the
8
9 literature. Furthermore, the performance of VS_2 at the anode side, particularly the
10
11 interaction at the anode/separator interfaces remain unexplored, despite the clear physical
12
13 advantageous. Also, coating VS_2 on the separators is a more simple and low-cost binder-
14
15 free modification strategy than coating the lithium metal surface. The facile coating
16
17 process on the polymer separator would facilitate the practical application and
18
19 commercial production of Li-S batteries.^{33, 34}
20
21
22

23
24 Herein, a recyclable VS_2 hexagonal nanotowers (HVS) double-side-modified
25
26 commercial polypropylene (PP) separator (D-HVS@PP separator) was fabricated *via* a
27
28 single-step hydrothermal method and subsequent vacuum filtration (Figure S1). The
29
30 fabricated D-HVS@PP separator kept both the “sulfiphilic” and “lithiophilic” features,
31
32 which can simultaneously trap Li_2S_x and suppress lithium dendrites. In addition, due to
33
34 the hexagonal tower-form nanostructure of the HVS, the D-HVS@PP separator also
35
36 exhibited a high-flux lithium-ion diffusion with improved mechanical strength. As a
37
38 result, the elaborate separator delivered high charge/discharge capacity and stable cycling
39
40 performance in Li-S batteries, even under high sulfur loading/lean-electrolyte conditions
41
42 with the controlled N/P ratio and when used in the pouch Li-S and lithium metal battery
43
44 systems.
45
46
47

48 49 **RESULTS AND DISCUSSION**

50
51
52
53
54
55
56
57
58
59
60

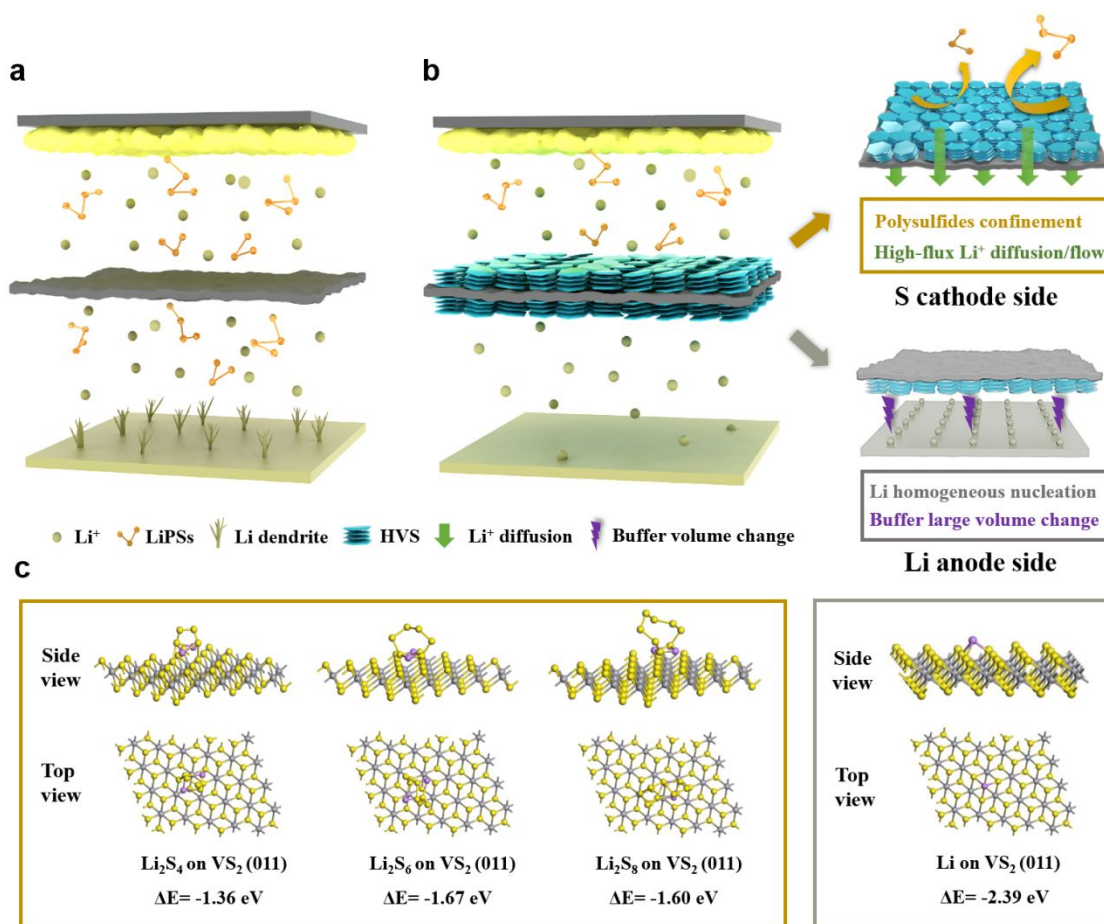


Figure 1. Working mechanism and theory simulation. Schematic illustrations of the working principle of the Li-S battery with (a) PP and (b) D-HVS@PP separator. (c) Density functional theory (DFT) calculation of the absorption energies of Li_2S_4 , Li_2S_6 , Li_2S_8 and Li on VS_2 (011) facet (Vienna *Ab-initio* Simulation Package (VASP)).

As illustrated in Figure 1, the commonly employed PP separator in conventional Li-S batteries guarantees the primary functions for the efficient migration of lithium ions and the isolation of the counter electrodes. However, it can hardly restrain the polysulfide shuttle, and Li dendrites growth (Figure 1a).^{16, 24} In the current work, an “amphiphilic” HVS material was introduced onto both sides of the PP separator, simultaneously realizing the distinct functionalities for the anode and cathode (Figure 1b). In the sulfur cathode side, the HVS can effectively prevent the shuttled Li_2S_x from passing through the

1
2
3 separator due to the strong chemical interactions. The designed layer-by-layer stacked
4 nanostructure of the HVS also creates the abundant channels and spaces for high-flux ion
5 diffusion/flow and provides enough exposed active sites for polysulfide adsorption. In
6 addition, the intrinsic metallic nature of the HVS can further reduce the interfacial
7 resistance between the electrode and the separator, enabling low polarization and fast
8 sulfur conversion kinetics³⁵. In the lithium anode side, the strong lithiophilic ability and
9 high electronic conductivity of the HVS can induce ions/electrons to
10 uniformly distribute at anode/separator interfaces, avoiding the formation of lithium
11 dendrites caused by the local charge concentration.³⁶⁻³⁸ At the same time, the stable
12 hexagonal tower-shaped architecture of the HVS is also beneficial to buffer the large
13 volume change of lithium metal under deep cycling and serves as a physical shield to
14 resist the lithium dendrites growth.^{18, 39} Hence, the D-HVS@PP separator can boost an
15 obvious enhancement in battery performance, and the detailed reasons have been
16 analyzed and discussed in the following sections.

17
18
19
20
21
22
23
24
25
26
27
28
29
30
31
32
33
34
35
36
37
38
39
40
41
42
43
44
45
46
47
48
49
50
51
52
53
54
55
56
57
58
59
60
The growth process and structural characterizations of the HVS were investigated in
Figure S2-6. Firstly, the scanning electron microscopy (SEM) images at various stages of
the hydrothermal process are displayed in Figure S2, where the possible formation
mechanism of the VS₂ hexagonal nanotowers is also schematically illustrated. PVP, as a
surfactant, is playing a crucial role with dual functions of the hexagonal tower-shaped
nanostructure.⁴⁰ First, it serves as a linking agent to bridge adjacent VS₂ nanoflakes
together, leading to the self-assembly of the nanoflake subunits along the c-axis. Second,
it plays a vital role on controlling the size and morphology of each VS₂ nanoflake along
the ab-plane, leading to the formation of a perfect hexagonal nanostructure instead of the

1
2
3 conventional VS₂ microflowers (MVS).^{32, 41, 42} The high-resolution transmission electron
4 microscopy (HRTEM), X-ray diffraction (XRD) and X-ray photoelectron spectroscopy
5 (XPS) analysis in Figure S3-5, showed that both HVS and MVS samples possessed the
6 same crystalline phase (JCPDS No. 89-1640), valence state and chemical composition,
7 belonging to the typical VS₂ structure. However, the higher intensity of the XRD peaks
8 and the perfect interlayer structure appears in the HRTEM images suggests that HVS is of
9 longer crystalline order. The HVS exhibited a Brunauer-Emmett-Teller (BET) surface
10 area of 31.4 m² g⁻¹, which is over 5 times higher than the MVS (5.8 m² g⁻¹), since the
11 multi-layered tower-like nanostructure was conducive to the exposure of more
12 micro/mesopores (10~70 Å) (Figure S6). The higher surface area allows the separator to
13 store more electrolyte and contribute more active sites, facilitating high-flux lithium-ion
14 diffusion and efficient interfacial reactions.^{43, 44}

15
16
17
18
19
20
21
22
23
24
25
26
27
28
29
30
31 In addition, to evaluate the amphiphilic functional property of the HVS separator, the
32 absorption energies of VS₂ (011) main facet towards the soluble Li₂S_x and metallic
33 lithium were calculated by density functional theory (DFT) simulations. As shown in
34 Figure 1c, the binding energies between VS₂ (011) facet and Li₂S₄, Li₂S₆ and Li₂S₈ were -
35 1.36, -1.67 and -1.60 eV, respectively, much higher than that between graphene and Li₂S₄
36 (-0.56 eV) (Figure S7). This confirmed that VS₂ possesses strong absorption ability for
37 Li₂S_x, especially longer-chained Li₂S₆ and Li₂S₈. Long-chained Li₂S_x are easier to
38 dissolve and shuttle in the electrolyte and result in the rapid capacity decay of Li-S
39 batteries.⁷ Notably, VS₂ also showed high chemical affinity (-2.39 eV) for metallic
40 lithium because of the strong interaction between Li and S atoms. This “sulfiphilic” and
41
42
43
44
45
46
47
48
49
50
51
52
53
54
55
56
57
58
59
60

“lithiophilic” property emphasizes the potential ability of VS_2 to trap Li_2S_x and suppress lithium dendrites simultaneously.

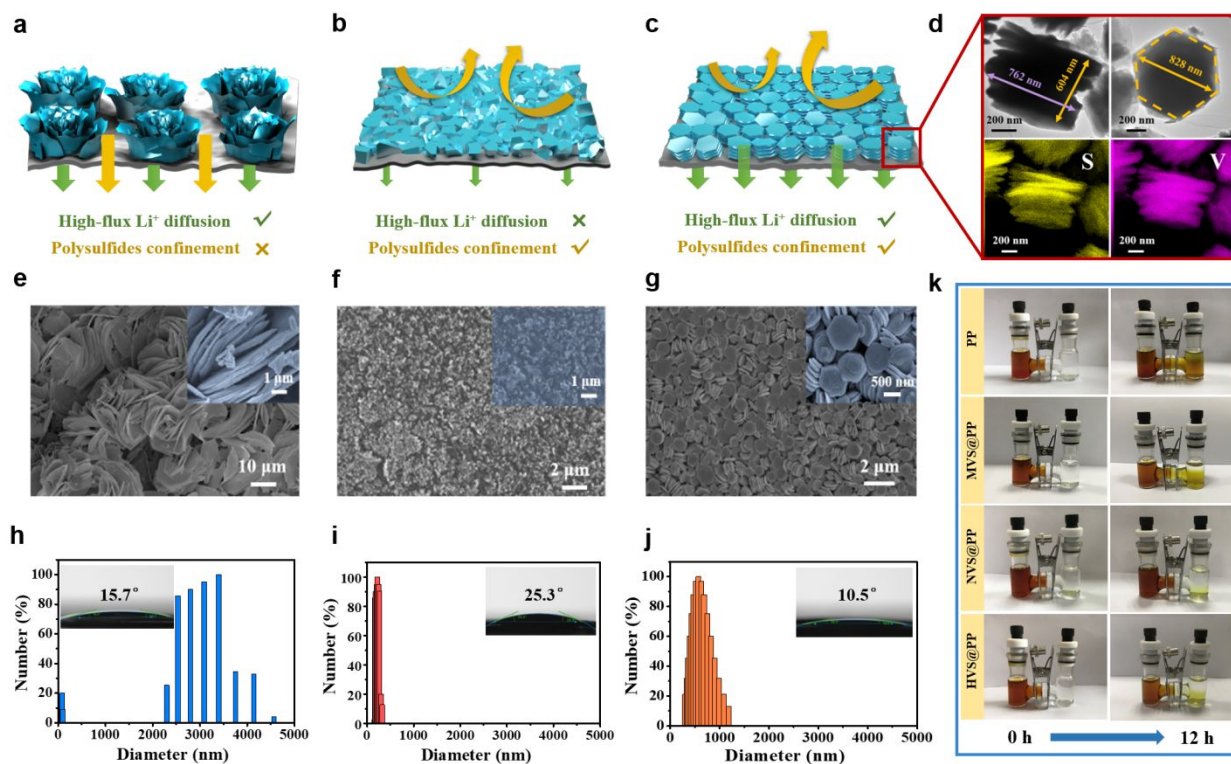


Figure 2. Functional description of different VS_2 modified separators on sulfur cathode side. Functional illustrations of the (a) MVS@PP, (b) NVS@PP and (c) HVS@PP separators on sulfur cathode side. (d) Transmission electron microscopy (TEM) images and element distribution of the VS_2 hexagonal nanotowers. SEM images of (e) MVS@PP, (f) NVS@PP and (g) HVS@PP separators. Particle size distributions and contact angle images (inset) for (h) MVS@PP, (i) NVS@PP and (j) HVS@PP separators, Li-S electrolyte as a test liquid was used in contact angle tests. (k) Diffusion tests of Li_2S_6 with PP, MVS@PP, NVS@PP and HVS@PP separators.

Before verifying the performance of the double-sided treated separator (D-HVS@PP) for the sulfur cathode or the lithium anode, a single-sided HVS@PP separator was first

1
2
3 tested to investigate the reactions at one electrode and eliminate the possible influence
4 from counter electrode. Firstly, three different VS₂ modified separators (MVS@PP, VS₂
5 nano-bulks (NVS)@PP and HVS@PP separators) were compared. As shown in Figure
6 2a, e and h, the MVS@PP separator is beneficial to achieve high-flux lithium-ion
7 diffusion, due to the high electrolyte affinity of VS₂ itself and the large particle sizes
8 (diameter 2000~5000 nm) of the MVS structure. As a result, the MVS@PP separator
9 exhibited a much smaller contact angle (15.7°) compared with the pure PP separator
10 (37.0°) (Figure S8a). However, the MVS@PP separator can hardly resist the Li₂S_x
11 diffusion because of the large microporous gaps among particles and low surface area of
12 MVS (Figure 2k). Also, the flower-shaped structure and the large particle sizes reduce
13 the contact area between MVS and the PP substrate, leading to the uneven distribution
14 and weak adhesive strength between the components of the MVS@PP (Figure S8b). The
15 second tested separator was NVS@PP (Figure 2b, f, i and k and Figure S9), in which
16 NVS were obtained by directly sonicating the HVS. The NVS particles were less than
17 500 nm in diameter, which means it could be densely loaded onto the PP separator and
18 effectively suppress Li₂S_x shuttle. However, NVS particles formed a blocking layer on the
19 PP substrate that significantly lowers the electrolyte wettability and hinders the lithium-
20 ion diffusion/flow. For HVS@PP separators, it can be seen that most of the nanotowers
21 are aligned vertically on the separator with the hexagonal layers parallel to the surface
22 (Figure 2g and Figure S10), which may be due to the more stable hexagonal 2D planes
23 and larger plane/height ratio of the as-prepared VS₂ nanotowers.^{45, 46} Due to the moderate
24 particle sizes (400~1200 nm), well-designed hexagonal tower-like structure and the high
25 surface area of the HVS, HVS@PP separators (Figure 2c, d, g and j) are able to guarantee
26
27
28
29
30
31
32
33
34
35
36
37
38
39
40
41
42
43
44
45
46
47
48
49
50
51
52
53
54
55
56
57
58
59
60

the adequate contact area and strong electrostatic interaction for HVS to be tightly linked to the separator (Figure S8b-d).^{45, 47} HVS also provided abundant tiny channels on the separator surface for both lithium-ion diffusion/flow and Li_2S_x suppression (Figure 2k).

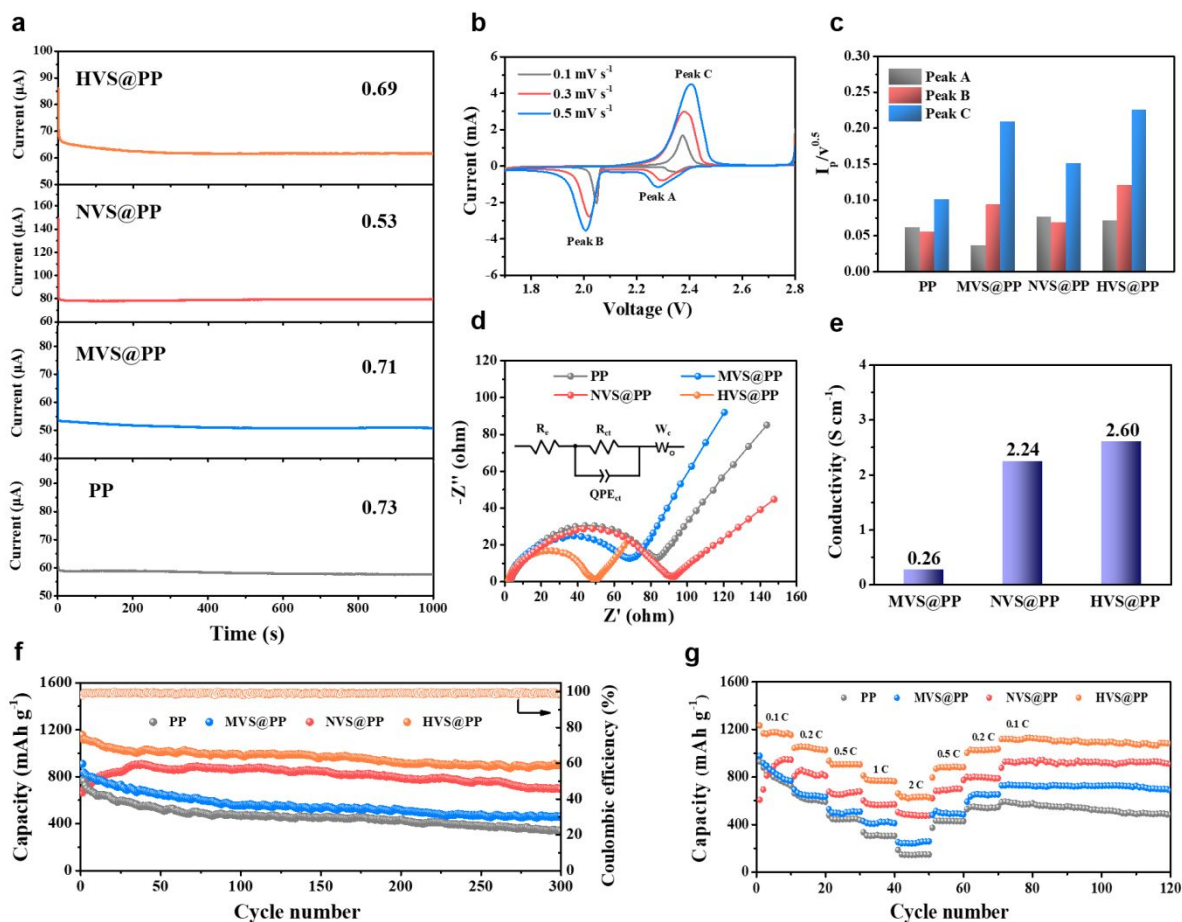


Figure 3. Electrochemical performance towards sulfur cathode side. (a) Lithium-ion transference numbers for the PP, MVS@PP, NVS@PP and HVS@PP separators tested by Li || Li symmetric cells. (b) CV plots of the HVS@PP separator at various scan rates within a potential window of 1.7 V-2.8 V (vs. Li/Li^+). (c) Values of CV peak current (I_p)/square root of the scan rates ($v^{0.5}$) for the four different separators in the first (peak A: $\text{S}_8 \rightarrow \text{Li}_2\text{S}_x$) and second (peak B: $\text{Li}_2\text{S}_x \rightarrow \text{Li}_2\text{S}_2/\text{Li}_2\text{S}$) cathodic reduction processes and the anodic oxidation process (peak C: $\text{Li}_2\text{S}_2/\text{Li}_2\text{S} \rightarrow \text{S}_8$). (d) EIS curves tested at open-circuit voltage for the four different separators,

1
2
3 inset: equivalent circuit model. (e) Electrical conductivities for the MVS@PP, NVS@PP and
4 HVS@PP separators. (f) Long-term cycling performance of the four different separators at 0.2 C
5
6 for 300 cycles. (g) Rate performance of the four different separators from 0.1 C to 2 C.
7
8
9

10 To evaluate the electrochemical performance of various separators towards the sulfur
11 cathode, a series of characterizations were further carried out in a coin-type configuration
12 (Figure 3). Firstly, the lithium-ion transference numbers (t_{Li^+}), defined as the ratio of
13 steady-state current to initial current, of various separators were calculated at a potential
14 of 10 mV.⁴⁶ The t_{Li^+} represents the ratio of the total charge carried by lithium ions to that
15 carried by both the lithium ions and the anions in the electrolyte, thus reflecting the
16 lithium-ion transport property of various separators.^{48, 49} The t_{Li^+} value of the MVS@PP
17 (0.71) and HVS@PP separators (0.69) are comparable to that of the pure PP separator
18 (0.73). NVS@PP, on the other hand, has the lowest lithium-ion transference numbers
19 (0.53). The low t_{Li^+} value suggesting the dense NVS functional layer covering on the
20 separator surfaces produced a stronger binding for lithium ions, which is unfavorable to
21 lithium-ion transport and conductivity.^{46, 49} This is also consistent with the results and
22 previous analysis in Figure 2.
23
24
25
26
27
28
29
30
31
32
33
34
35
36
37
38
39

40 Next, cyclic voltammetry (CV) and electrochemical impedance spectra (EIS) were
41 collected to investigate the lithium-ion transfer rates across various separators. Since fast
42 lithium-ion diffusion facilitates the sulfur conversion kinetics in Li-S battery system, the
43 effective lithium-ion diffusion rates of different VS₂ separators can be acquired by
44 investigating the CV curves at various scan rates. For the CV plots of all the separators
45 (Figure 3b and Figure S11), there are two reduction peaks and one oxidation peaks. The
46 first peak (peak A: ~2.3 V) and the second peak (peak B: ~2.0 V) in the cathodic scan
47
48
49
50
51
52
53
54
55
56
57
58
59
60

1
2
3 represent the reduction of sulfur to soluble Li_2S_x ($\text{S}_8 \rightarrow \text{Li}_2\text{S}_x$) and the formation of solid
4 lithium sulfides ($\text{Li}_2\text{S}_x \rightarrow \text{Li}_2\text{S}_2/\text{Li}_2\text{S}$). The anodic oxidation peak (peak C: ~ 2.4 V)
5
6 corresponds to the reversible transition from lithium sulfides to sulfur ($\text{Li}_2\text{S}_2/\text{Li}_2\text{S} \rightarrow \text{S}_8$).
7
8 According to the Randles-Sevcik equation,^{30, 50} the peak current (I_p) has a linear relation
9
10 with the square root of the scan rate ($v^{0.5}$) for all separators (Figure S12). The lithium-ion
11
12 diffusion rate (D_{Li^+}) can be calculated by the slope of the fitted line ($I_p/v^{0.5}$). As can be
13
14 concluded from Figure 3c and Table S1, the VS_2 modified separators at different peaks
15
16 showed enhanced lithium-ion diffusion rates compared with the pure PP separator. The
17
18 existed VS_2 at the cathode/separator interfaces accelerates the redox process of insulated
19
20 lithium sulfides and prevents them from depositing in the voids of the separators,
21
22 ensuring facile lithium-ion diffusion. Benefiting from the high electrolyte affinity and the
23
24 abundance of active sites, the HVS@PP separator exhibited the fastest lithium-ion
25
26 diffusion rates among all the VS_2 modified separators. Notably, the NVS@PP separator
27
28 displayed the fastest lithium-ion diffusion at peak A, suggesting the efficient reduction
29
30 from sulfur to Li_2S_x . Nevertheless, it could hardly provide enough sites for the reversible
31
32 conversion of lithium sulfides because of the dense NVS layer, consequently leading to
33
34 lower lithium-ion diffusion rate at peaks B and C. The EIS curves of the various
35
36 separators at open-circuit voltage were further displayed in Figure 3d, where all the
37
38 Nyquist plots were composed by a high-frequency semicircle and a low-frequency sloped
39
40 line, attributing to the charge transfer resistance (R_{ct}) and mass-diffusion process,
41
42 respectively.^{44, 51} Based on the fitted equivalent electrical circuit model, the calculated
43
44 impedance data are summarized in Table S2. The R_{ct} value of the HVS@PP separator
45
46 (45.8 Ω) was lower than that of the PP (71.7 Ω), MVS@PP (56.3 Ω) and NVS@PP (87.2
47
48
49
50
51
52
53
54
55
56
57
58
59
60

1
2
3 Ω) separators. This result verified the faster faradic reaction kinetics and smoother charge
4 transfer of the HVS@PP separator, consistent with the above analysis.^{44, 52}
5
6

7
8 Beside the lithium-ion transference, the conductivity is another vital factor to affect
9 battery performance.^{53, 54} The NVS@PP (2.24 S cm⁻¹) and HVS@PP (2.60 S cm⁻¹)
10 separators exhibited an almost tenfold higher surface conductivity compared with the
11 MVS@PP separator (0.26 S cm⁻¹) (Figure 3e), as the microscale flower-shaped structure
12 of MVS could not uniformly distribute on the PP separator surfaces to ensure continuous
13 electron transfer (Figure S8b). It has been proved that a higher surface conductivity of a
14 separator can lower the cathode/separator interfacial resistance, facilitating low
15 polarization (Figure S13) and fast sulfur conversion during charge/discharge processes.^{35,}
16
17
18
19
20
21
22
23
24
25

26 54

27
28 Following the above-detailed analyses on structure and function, the practical cycling
29 performance of various VS₂ modified separators in Li-S batteries was investigated, and
30 the results are shown in Figure 3f. Due to both the fast ion/electron diffusion and effective
31 Li₂S_x suppression, the HVS@PP separator delivered the highest initial discharge capacity
32 of 1156 mAh g⁻¹ at 0.2 C (1 C=1675 mAh g⁻¹ in Li-S battery). The discharge capacity was
33 maintained at 908 mAh g⁻¹ with stabilized Coulombic efficiency (~99 %) and slow
34 capacity attenuation (0.072 % per cycle) after 300 cycles. The NVS@PP separator, on the
35 other hand, exhibited the lowest initial discharge capacity of 665 mAh g⁻¹ with a
36 gradual capacity rising in the first 40 cycles derived from the electrochemical
37 activation,^{20, 55, 56} due to the dense NVS layer that hindered the lithium-ion diffusion/flow.
38
39
40
41
42
43
44
45
46
47
48
49
50
51
52
53
54
55
56
57
58
59
60

1
2
3 separators, proving that suppressing Li_2S_x shuttle is more crucial to maintain the stable
4 cycle capacity in Li-S batteries. In addition, the HVS@PP separator also yielded the best
5 rate performance among all separators (Figure 3g). When the current density was
6 increased to 2 C, the HVS@PP separator still delivered a high discharge capacity of 630
7 mAh g^{-1} , reaffirming the low polarization and the fast reaction kinetics of the HVS@PP
8 separator due to the improved ion/electron transferability at the cathode/separator
9 interface.
10
11
12
13
14
15
16
17
18

19 A series of post-mortem analyses were further conducted better to evaluate the practical
20 cycling stability of the HVS@PP separator. As shown in Figure S14, the HVS@PP
21 separator still maintained the hexagonal tower-form structure after 300 cycles, proving its
22 high stability in coping with the repeated charging and discharging. EIS plots for the
23 HVS@PP separator after various cycles are also presented in Figure S15, with the
24 corresponding impedance data listed in Table S2. The R_{ct} value of the HVS@PP separator
25 decreased from 45.8 Ω (fresh cell) to 13.5 Ω (after 50 cycles), and 6.3 Ω (after 300
26 cycles), suggesting a gradually enhanced charge conductivity with the increased number
27 of cycles, which is beneficial to the sulfur redox reaction kinetics in LSBs.^{7, 57} The
28 HVS@PP separator also displayed lower R_{ct} values than PP separator after 300 cycles,
29 confirming the superiority of the HVS layer for the fast charge transfer during cycling.
30
31 Finally, the sulfur content deposited on the lithium metal anodes for the various
32 separators after 300 cycles were quantitatively assessed by inductive coupled plasma-
33 atomic emission spectrometry (ICP-AES) (Figure S16). The lithium metal anode
34 assembled with the HVS@PP separator displayed the lowest sulfur content (5.1 ppm)
35 compared with pure PP, MVS@PP and NVS@PP separators (16.7, 13.4 and 6.7 ppm).
36
37
38
39
40
41
42
43
44
45
46
47
48
49
50
51
52
53
54
55
56
57
58
59
60

This excellent Li_2S_x suppression ability of the HVS@PP separator once again supports its stable cycling performance shown in Figure 3f.

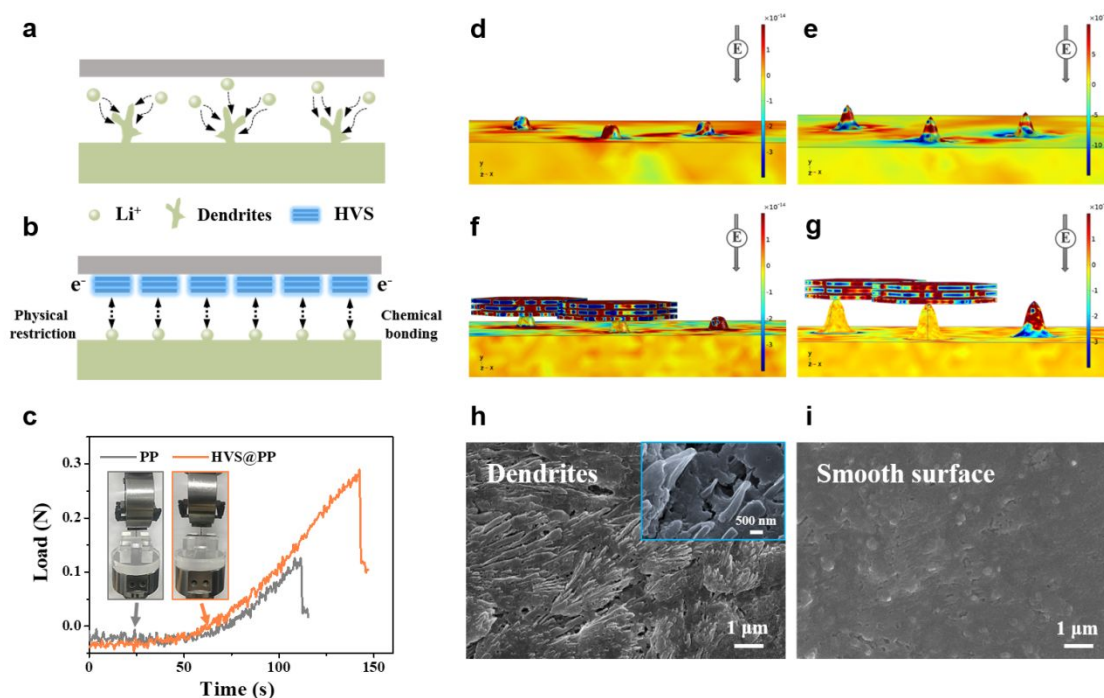


Figure 4. Schematics of lithium growth with different separators on lithium anode side. Functional illustrations of the (a) PP and (b) HVS@PP separators on lithium anode side. (c) Puncture strength tests of the PP and HVS@PP separators, inset: the PP and HVS@PP separators were fixed on a sample holder with a gap width of 8 mm for mechanical puncture tests. Finite element method (FEM) using COMSOL Multiphysics for the simulation of the electric field distribution at different growth periods of (d and e) the lithium dendrites and (f and g) the lithium dendrites covered with the HVS layer. SEM images of the lithium metal anodes with (h) PP and (i) D-HVS@PP separators after stripping/plating for 100 cycles.

Motivated by the excellent performance of the HVS grown on PP (HVS@PP), we then investigated the performance of the double-sided HVS@PP separator for lithium metal anode using various simulation and electrochemical spectroscopic techniques (Figure 4). For clarity, the mechanisms of lithium growth for the three different separators are

1
2
3 illustrated schematically. For pure PP separator (Figure 4a), it can hardly cope with both
4 the lithium dendrite growth and the volumetric change of bare lithium metal during
5 repeated stripping/plating cycles. Because of the unevenly distributed charges, lithium
6 ions also tend to aggregate near the dendrites and further accelerate the dendrite growth,
7 leading to a severe consumption of electrolyte and the fragmentation of solid electrolyte
8 interphase (SEI) layer.^{11, 58} In contrast, the homogeneous lithium nucleation and growth
9 can be achieved when an HVS layer modifies the surface of the PP separator facing the
10 lithium metal anode for the following reasons (Figure 4b): (a) “Lithiophilic” feature of
11 the HVS (Figure 1c) provides a high chemical affinity with lithium, which can effectively
12 alleviate the dendrite spread and prevent the formation of “dead lithium” during
13 cycling.^{36, 59} (b) The stable hexagonal multi-layered nanostructure of the HVS not only
14 accommodate Li deposition and buffers volume expansion of lithium metal during
15 cycling but also improves the puncture resistance of the PP separator to physically resist
16 the lithium dendrite growth (Figure 4c).^{18, 24, 39} (c) The improved interfacial conductivity
17 between the separator and the lithium anode ensures homogeneous electric field
18 distribution and decreases the current density, thus conducive to the homogeneous
19 nucleation and the suppression of lithium dendrites growth.^{38, 60}

20
21
22
23
24
25
26
27
28
29
30
31
32
33
34
35
36
37
38
39
40
41
42 To shed more light on the lithiation process, the COMSOL Multiphysics technique was
43 adopted to simulate the electric field distribution at different growth periods of the lithium
44 dendrites with or without an HVS covering layer (Figure 4d-g and Figure S17).^{59, 61} For
45 the bare lithium metal anode, the electric field intensity around the dendrites dramatically
46 increases (visible in red) with the extremely uneven electric field distribution. This
47 demonstrates that lithium ions are more likely to be focused at the formed dendrites due
48
49
50
51
52
53
54
55
56
57
58
59
60

1
2
3 to the tip effect, further leading to the continuous growth of lithium dendrites.
4
5 Nevertheless, when the lithium dendrites are covered with the conductive HVS layer, the
6
7 gathered electric fields around the dendrites are dispersed by the multi-layered HVS
8
9 structure to form a more uniform distribution on the surface of lithium anode. Hence, the
10
11 tip effect or hotspot around the lithium dendrites is eliminated.
12
13

14
15 The lithium metal anodes for different separators were further studied after 100 cycles
16
17 using SEM (Figure 4h and i) and atomic force microscopy (AFM) (Figure S18), to
18
19 evaluate the practical suppression effect of the D-HVS@PP separator on the lithium
20
21 dendrites growth. The lithium anode exhibited a quite rough surface with plenty of
22
23 needle-shaped dendrites when PP separator was used. Conversely, the D-HVS@PP
24
25 separator maintained a smooth lithium anode surface. The results further confirm the
26
27 effectiveness of the D-HVS@PP separator in suppressing the dendrite growth as analyzed
28
29 previously.
30
31
32
33
34
35
36
37
38
39
40
41
42
43
44
45
46
47
48
49
50
51
52
53
54
55
56
57
58
59
60

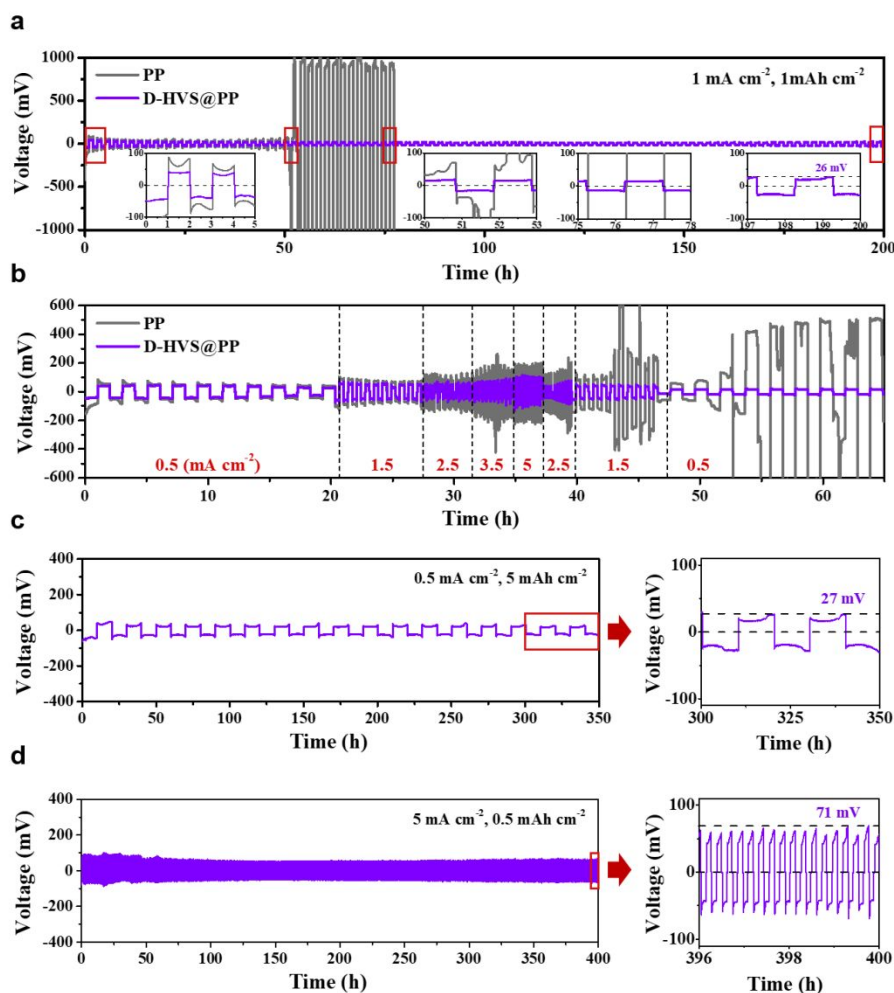


Figure 5. Electrochemical performance towards lithium anode side. (a) The voltage profiles in Li || Li symmetric cells with PP and D-HVS@PP separators at 1 mA cm⁻² with a stripping/plating capacity of 1 mAh cm⁻². (b) Rate performance of the symmetric cells with PP and D-HVS@PP separators at a stripping/plating capacity of 0.5 mAh cm⁻². The voltage profiles in Li || Li symmetric cells with D-HVS@PP separator: (c) at 0.5 mA cm⁻² with a stripping/plating capacity of 5 mAh cm⁻² and (d) at 5 mA cm⁻² with a stripping/plating capacity of 0.5 mAh cm⁻².

Galvanostatic cycling performances of Li || Li symmetric cells with the PP and D-HVS@PP separators were investigated to evaluate the stability of lithium

1
2
3 stripping/plating with different separators (Figure 5). Based on the voltage profiles in
4
5 Figure 5a, the pure PP separator exhibited an initial overpotential of 89 mV, twice higher
6
7 than the D-HVS@PP separator (41 mV). In addition, the polarization for the pure PP
8
9 separator showed a sharp increase to nearly 1000 mV after 50 h, which might be
10
11 attributed to the excessive formation of ‘dead’ lithium on the surface of lithium metal
12
13 resulting in the fragmentation of SEI layer and unstable Li/electrolyte interface
14
15 accompanying with poor electrical connection.^{25, 36} In contrast, the D-HVS@PP separator
16
17 maintained a flat lithium stripping/plating plateau with a low overpotential of 26 mV even
18
19 after 200 h. During the switch of different current densities from 0.5 mA cm⁻² to 5 mA
20
21 cm⁻² and reverted to 0.5 mA cm⁻² (Figure 5b), the D-HVS@PP separator also displayed a
22
23 more stable polarization vibration compared with the pure PP separator, further indicating
24
25 its enhanced rate performance in symmetric cells. Even at a larger stripping/plating
26
27 capacity of 5 mAh cm⁻² (Figure 5c) or a higher current density of 5 mA cm⁻² (Figure 5d),
28
29 the symmetric cells with the D-HVS@PP separator still exhibit stable voltage profiles
30
31 (~27 mV for 350 h or ~71 mV for 400 h). All the results confirm D-HVS@PP separator
32
33 can facilitate the uniform lithium nucleation and growth due to the synergistic effect of
34
35 the effective chemical/physical restriction and the improved interfacial conductivity,
36
37 subsequently achieving the high cycling stability of lithium metal anode.
38
39
40
41
42
43
44
45
46
47
48
49
50
51
52
53
54
55
56
57
58
59
60

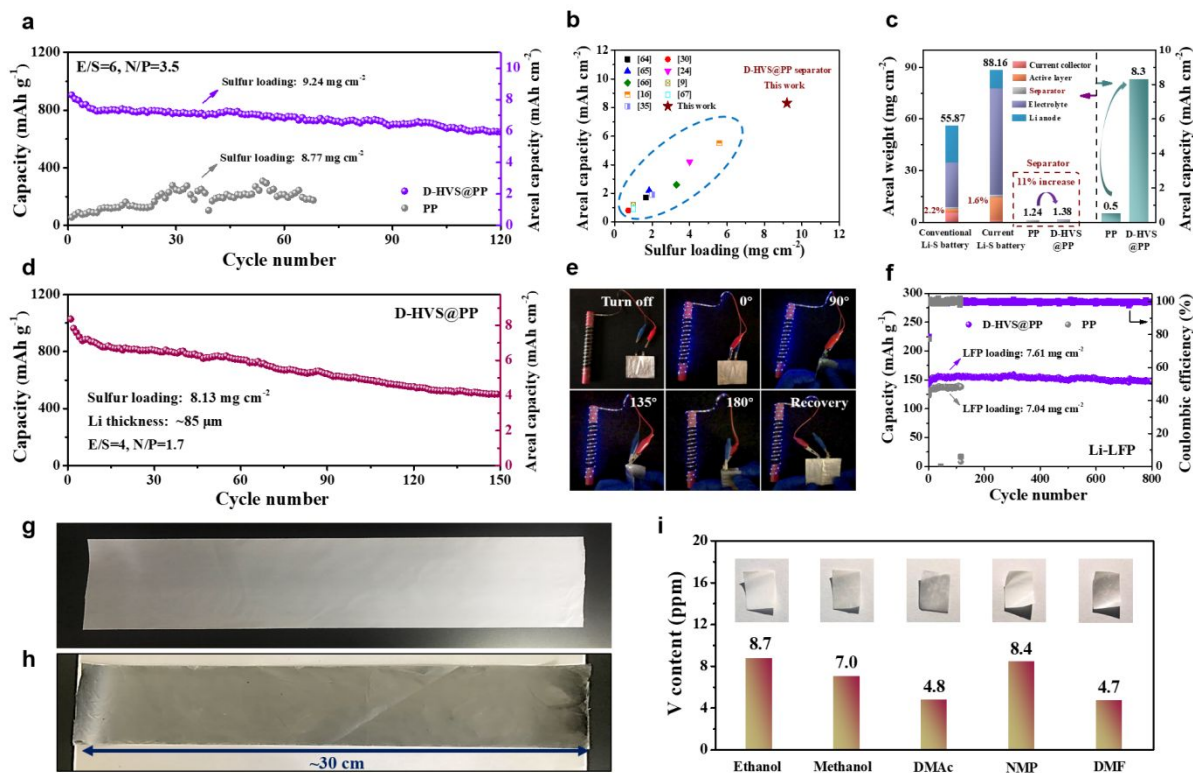


Figure 6. Performance of various battery configurations using different separators. (a) Cycling performance of PP and D-HVS@PP separators under high sulfur-loading and lean-electrolyte conditions at 0.2 C. (b) Comparison of the areal capacities of D-HVS@PP separator at a high sulfur loading with that of other reported similar materials in Li-S battery, more details are shown in Table S4. (c) Comparison of both the areal weight and areal capacity of PP and D-HVS@PP separators. (d) Cycling performance of D-HVS@PP separators under a lower E/S and N/P ratios at 0.2 C. (e) LEDs illuminating test by a Li-S pouch cell using the D-HVS@PP separator in various folded states. (f) The cycling performance of PP and D-HVS@PP separators in the Li-LiFePO₄ (LFP) batteries. (g) Image of the commercial PP separator. (h) The large-scale fabrication of D-HVS@PP separator. (i) The vanadium content of the various organic solvents (10 mL) after the recycling experiments of D-HVS@PP separator probed by ICP-AES, inset: the corresponding separator photos after the recycling treatment.

1
2
3
4
5
6
7
8
9
10
11
12
13
14
15
16
17
18
19
20
21
22
23
24
25
26
27
28
29
30
31
32
33
34
35
36
37
38
39
40
41
42
43
44
45
46
47
48
49
50
51
52
53
54
55
56
57
58
59
60

Despite numerous efforts made to the development of advanced functional separators, most of the studies focused solely on the high capacity performance and ignored the consideration of sulfur loadings and electrolyte utilization^{4, 20}. A low sulfur areal loading (<2.0 mg cm⁻²) and high electrolyte/sulfur (E/S) ratio (>15 mL g⁻¹) can hardly achieve competitive areal capacities and energy density with that of the state-of-art Li-ion batteries²⁰. Accordingly, the D-HVS@PP separator with a high sulfur-loading (9.24 mg cm⁻²) S/carbon nanofibers (CNFs) cathode and a ~200 μm thick lithium anode (Figure S19a) was employed under a lean-electrolyte condition (6 mL g⁻¹) to explore its potential for practical use. The negative to positive capacity ratio (N/P) for this assembled Li-S battery was calculated to be 3.5 (Table S3).^{62, 63} Despite the relatively high polarization, which is due to the improved sulfur loading and the low E/S ratio, the D-HVS@PP separator maintained stable charging/discharging platform and excellent areal capacity of 6.0 mAh cm⁻² even after 120 cycles. The improved cycle stability can be attributed to the unique amphiphilic property, the high surface conductivity, and the superior electrolyte penetration for Li⁺ transfer (Figure 6a and Figure S20). Notably, the D-HVS@PP has achieved an initial capacity of 8.3 mAh cm⁻², which is over 16 times higher than the PP separator (0.5 mAh cm⁻²) under similar conditions. The high initial area capacity and the excellent cyclic stability of the D-HVS@PP separator also outperforms other similarly reported materials applied as separators, cathodes or interlayers in Li-S batteries (Figure 6b and Table S3).^{9, 16, 24, 30, 35, 64-67} This performance was achieved just at the expense of an 11% increase in the separator weight (0.14 mg cm⁻²), accounting for only 0.24% in the basic units of conventional Li-S battery or even lower (0.18%) in the current high sulfur-loading battery system (Figure 6c and Table S5). Furthermore, considering that a thinner

1
2
3 Li anode and a controlled N/P ratio are more relevant to the practical applications of Li-S
4 batteries, the cycling performance of D-HVS@PP separator was further investigated
5 under more strict conditions; *i.e.* with a $\sim 85 \mu\text{m}$ thick lithium anode (Figure S19b) and
6 the lower N/P (1.7) and E/S (4 mL g^{-1}) ratios (Figure 6d). The battery with D-HVS@PP
7 separator can still deliver a high cell-level gravimetric energy density of $327 \text{ Wh kg}_{\text{cell}}^{-1}$
8 (the detailed calculations are shown under Table S5) and favourable stability for 150
9 cycles closed to the battery in Figure 6a. All these results prove the feasibility of the D-
10 HVS@PP separator in practical Li-S cells.
11
12

13
14
15 Furthermore, to achieve wider application visibility, we verified the separator stability
16 in flexible devices. A Li-S pouch cell was assembled using S/CNFs cathode, D-HVS@PP
17 separator, $\sim 200 \mu\text{m}$ thick lithium anode and vacuum-sealed aluminium-plastic film, with
18 an E/S ratio of 6 mL g^{-1} and an N/P ratio of 3.4. The flexible battery was directly applied
19 in practical light-emitting diodes (LEDs) illumination tests without any additional
20 pressure effect (Figure 6e). This pouch cell exhibited a high open-circuit voltage of 2.45
21 V with low self-discharge (Figure S21), and can steadily power an array of LEDs in
22 various folded states from 0° (flattened) to 180° (folded) and back to 0° (flattened), and
23 even when repeatedly bent (Movie S1). Apart from the Li-S battery system, the D-
24 HVS@PP separator can also be extended to apply in the Li-LiFePO₄ (LFP) batteries
25 assembled with an LFP cathode and a lithium metal anode (Figure 6f). Due to the high
26 charge conductivity, high electrolyte affinity and homogeneous lithium nucleation, the Li-
27 LFP battery with D-HVS@PP separator can deliver a stable discharge capacity of 148.1
28 mAh g^{-1} and areal capacity of 1.13 mAh cm^{-2} at 1 C (1 C = 170 mAh g^{-1} for LFP cathode)
29 even after 800 cycles. These values are higher than that recorded for the conventional PP
30
31
32
33
34
35
36
37
38
39
40
41
42
43
44
45
46
47
48
49
50
51
52
53
54
55
56
57
58
59
60

separator (138.2 mAh g⁻¹ and 0.97 mAh cm⁻², short circuit after 100 cycles), further highlighting the potential of the D-HVS@PP separator in broader application fields. Notably, compared with the performance for Li-S batteries in Figure 6a and d, the lower but more stable cycling performance of Li-LFP battery is attributed to the distinct insertion/extraction lithium storage mechanism of LiFePO₄ cathode and its well-known high stability benefiting from the strong support of phosphate group in its lattice structure.

In addition to the universality, the large-scale fabrication and the recyclability of functional materials are other significant factors for practical and commercially viable separator materials. The D-HVS@PP separator can be simply prepared by one-step hydrothermal technique followed by vacuum filtration, hence easy to be commercialized and applied in the mass production of the D-HVS@PP separator. To further proof, we have prepared a thirty-centimetre-long D-HVS@PP separator through a large-area continuous filtration method (Figure 6g and h). Moreover, considering the cost and toxicity of VS₂ materials,⁶⁸ recycling tests were also carried out with the D-HVS@PP separator in various common organic solvents (Figure 6i). The HVS functional materials could be utterly separated from the PP separator to ethanol solvent with an assisted physical vibration, which may be attributed to the higher wettability of ethanol solvent towards PP separator. The recycled vanadium solution can be applied to the reproduction of the D-HVS@PP separator or some other aspects.

CONCLUSIONS

We designed a double-faces separator based on coating commercial PP membrane with 2D HVS (D-HVS@PP) *via* a facile and easy to scale up strategy to simultaneously solve different kinds of problems for the practicality of Li-S batteries. The prepared separator was subjected to a

1
2
3 comprehensive characterization program combining with the DFT calculation and COMSOL
4 Multiphysics simulation. The materials spectroscopic and computational characterization
5 confirmed the excellent physical, chemical, and electrochemical properties of the D-HVS@PP
6 when used as a separator in Li-S batteries, *e.g.* the “amphiphilic” nature for both Li_2S_x and pure
7 lithium, high electronic conductivity and special hexagonal tower-like nanostructure. For the
8 sulfur cathode, the HVS functional layer effectively suppressed the Li_2S_x shuttle and ensured the
9 fast interfacial electron transfer and the smooth lithium-ion diffusion through the separator. For
10 the lithium anode, it also promoted the uniform nucleation and growth of lithium and buffered
11 the volume expansion of lithium metal during repeated stripping/plating process. Hence,
12 compared with conventional PP separators, the D-HVS@PP separators enabled a high cell-level
13 gravimetric energy density of $327 \text{ Wh kg}_{\text{cell}}^{-1}$ with stable cycling even under the practically
14 relevant conditions of high sulfur loading, lean-electrolyte and low N/P ratio, or when applied in
15 flexible Li-S pouch and Li-LFP batteries. In particular, the large-scale fabrication and
16 recyclability of the D-HVS@PP separators are also evaluated to highlight its practicality further.
17 We expect this feasible and straightforward separator design can arouse more attention and
18 thoughts to boost the future commercialized development of the Li-S batteries and even other
19 advanced energy storage technologies.
20
21
22
23
24
25
26
27
28
29
30
31
32
33
34
35
36
37
38
39
40
41

42 **EXPERIMENTAL SECTION**

43
44 **Chemicals and materials.** All chemicals were of analytical grade and used without further
45 purification. Sodium metavanadate (NaVO_3), sublimed sulfur (S) and N-methyl-2-pyrrolidone
46 (NMP) were obtained from Aladdin. Thioacetamide (TAA) and ammonium hydroxide
47 ($\text{NH}_3 \cdot \text{H}_2\text{O}$) were purchased from Sinopharm Chemical Reagent Co. Ltd. Polyvinylidene fluoride
48
49
50
51
52
53
54
55
56
57
58
59
60

1
2
3 (PVDF) was obtained from Arkema. Lithium sulfide (Li_2S) was purchased from Sigma-Aldrich.
4
5 Poly(vinylpyrrolidone) (PVP K90) was supplied by BASF chemical company in Germany.
6

7
8 **Preparation of the VS_2 hexagonal nanotowers (HVS).** HVS was prepared using a one-step
9
10 hydrothermal technique. Firstly, 0.468 g NaVO_3 , 1.503 g TAA, 6 ml $\text{NH}_3\cdot\text{H}_2\text{O}$ and 30 ml
11
12 distilled water were mixed and magnetically stirred for 5 min. Secondly, 1 g PVP K90 was added
13
14 into the mixture; then the solution was stirred for another 40 min at ambient temperature. The
15
16 formed precursor solution was then transferred into a 50 ml Teflon-lined stainless-steel autoclave
17
18 and maintained at 180 °C for 10 h. After cooling, the precipitate was collected and washed
19
20 thoroughly with water and ethanol several times to recover the final HVS samples.
21
22

23
24 **Preparation of the VS_2 microflowers (MVS) and VS_2 nano-bulks (NVS).** MVS and NVS
25
26 samples were prepared for comparison. Conventional MVS were synthesized using the same
27
28 synthesis method as the HVS without the addition of PVP K90. NVS were obtained by
29
30 sonicating the as-prepared HVS in ethanol solution for 1 hour.
31
32

33
34 **Preparation of the HVS@PP, MVS@PP and NVS@PP separators.** The VS_2 modified
35
36 separators were prepared by direct vacuum filtration technology without using any binder. 2 mg
37
38 of the as-prepared sample (HVS, MVS or NVS) was dispersed in 20 ml ethanol. The resulting
39
40 suspensions were directly vacuum filtered onto a commercial PP separator and then dried at 60
41
42 °C in a vacuum oven for 6 hours, to form the targeted HVS@PP, MVS@PP and NVS@PP
43
44 separators, respectively.
45
46

47
48 **Preparation of the sulfur cathodes.** The sulfur slurry was prepared by ball-milling a mixture
49
50 of 280 mg sulfur powder, 80 mg Super P, 40 mg PVDF and 1.8 ml N-methyl-pyrrolidone (NMP)
51
52 for over 6 hours. The slurry was then coated to an aluminum foil and dried under vacuum at 60
53
54 °C for 12 hours to form the sulfur cathode. The sulfur mass loading is $\sim 1.5 \text{ mg cm}^{-2}$.
55
56
57
58
59
60

1
2
3 **Preparation of the Li₂S₆ solution.** 0.005 M Li₂S₆ solution (30 mM in sulfur) was obtained by
4 chemically reacting sulfur powder with Li₂S in 1,3-dioxolane/1,2-dimethoxyethane solution
5 (DOL/DME, 1:1 by volume).
6
7

8
9
10 **Characterization.** Morphological data and energy dispersive spectra (EDS) mapping were
11 obtained using a field emission scanning electron microscopy (FE-SEM) (GeminiSEM500,
12 China) and a transmission electron microscopy (TEM) (JEOL JEM2100, Japan). X-ray
13 diffraction (XRD) measurements were carried out using a PANalytical X'pert MPDPro
14 (Netherlands) diffractometer with a Cu Ka radiation source (40 kV, 40 mA). Brunauer–Emmett–
15 Teller (BET) surface areas and pore size distributions were obtained at -196 °C liquid nitrogen
16 temperature) using an ASAP 2020 (America) instrument. X-ray photoelectron spectroscopy
17 (XPS) measurements were carried out on a Kratos Axis Ultra (England) instrument using a
18 monochromatic Al Ka radiation source (150 W, 15 kV and 1486.6 eV) at 10⁻⁹ Torr pressure. The
19 contact angle images were obtained on a KRUSS DSA100 (Germany) instrument using Li-S
20 electrolyte as a test liquid. The accurate element contents (sulfur and vanadium) were acquired
21 with an inductively coupled plasma-atomic emission spectrometry (ICP-AES) (Shimadzu ICPE-
22 9000, Japan). The electric conductivities of various VS₂ modified separators were measured on a
23 four-point probe tester (2182A, America) with a testing current from 4 to 8 mA. Mechanical
24 puncture tests of the separators were carried out on an Instron 5548 (America) Micro Tester
25 Load Test Machine, where a lab-made sample holder with a gap width of 8 mm was used to fix
26 the tested separators, and the rate of compression displacement was set to be 1 mm min⁻¹. A
27 SOLVER NEXT (China) atomic Force Microscopy (AFM) was used to study the dendrite
28 growth on the lithium anode surfaces.
29
30
31
32
33
34
35
36
37
38
39
40
41
42
43
44
45
46
47
48
49
50
51
52
53
54
55
56
57
58
59
60

1
2
3 **Cell assembly and electrochemical measurements.** Coin-type (2032) and pouch cells were
4 assembled in an Ar-filled glovebox (DELLIX LS750S, China) with moisture and oxygen
5 contents below 1.0 ppm. For the Li-S batteries, the sulfur cathode and lithium-metal foil anode
6 were separated by various VS₂ modified PP separators. The electrolyte was composed of 1.0 M
7 lithium bis (trifluoromethanesulfonyl) imide (LITFSI) in a solvent mixture of DME/DOL (1 : 1
8 by volume) with 1.0 % LiNO₃ additive. The quantity of electrolyte was controlled at 10~15 μ L
9 per 1 mg sulfur. Galvanostatic charge/discharge tests were carried out using a LANHE battery
10 tester within a voltage window of 1.7~2.8 V (vs. Li/Li⁺). Cyclic voltammetry (CV) was
11 performed using a CHI 660D (China) electrochemical workstation in a voltage range of 1.7~2.8
12 V. Electrochemical impedance spectra (EIS) were obtained in a frequency range from 0.01 Hz to
13 100 kHz. In addition, the Li || Li symmetric cells were assembled with the various separators
14 sandwiched between two lithium electrodes. The Li-LFP coin-type batteries were constituted by
15 sandwiching separators between an LFP cathode and a ~200 μ m thick lithium anode. The
16 electrolyte was 1.0 M LiPF₆ in a solution of the ethylene carbonate and diethyl carbonate (1:1 by
17 weight).

18
19
20
21
22
23
24
25
26
27
28
29
30
31
32
33
34
35
36
37 **Computational method.** The density functional theory (DFT) calculation was performed
38 using the Vienna *Ab-initio* Simulation Package.^{69, 70} The electron-ion interaction was described
39 by projector augmented-wave (PAW) pseudopotentials. For the exchange and correlation
40 functionals, we use the Perdew-Burke-Ernzerhof (PBE) version of the generalized gradient
41 approximation (GGA) exchange-correlation.⁷⁰ In the DFT calculation, the (011) phase of VS₂
42 and the pure graphene were used to reveal the binding energy with polysulfide (*e.g.* Li₂S₄, Li₂S₆
43 and Li₂S₈). The vacuum layer thickness was set to 15 Å to avoid virtual interaction and obtain
44 more accurate results. The energy cutoff of 400 eV was used for the wave functions expansion.
45
46
47
48
49
50
51
52
53
54
55
56
57
58
59
60

1
2
3 The Brillouin zone integration was sampled with a $3 \times 3 \times 1$ k-grid mesh for geometry
4 optimization, and $5 \times 5 \times 1$ k-grid mesh for electronic properties calculations to achieve high
5 accuracy. The energy and force converged to 1.0×10^{-5} eV atom⁻¹ and 0.03 eV·Å⁻¹. The
6
7
8
9
10 corresponding binding energy (ΔE_{BE}) is defined as:

$$\Delta E_{BE} = E_{A+B} - E_A - E_B \quad (1)$$

11
12
13
14 Where the E_{A+B} is the total energy of the structure of the VS₂ (011) or graphene combined with
15 polysulfide, E_A is the total energy of the (011) phase of VS₂ or pure graphene, and E_B is the total
16
17
18
19
20
21
22
23 energy of the polysulfide (*e.g.* Li₂S₄, Li₂S₆ or Li₂S₈). Based on the definition, a more negative
24
25 value indicates a stronger binding system.

26
27
28
29
30
31
32
33
34
35
36
37
38
39
40
41
42
43
44
45
46
47
48
Finite element method (FEM) simulation. The electric field distribution in different growth
49
50
51
52
53
54
55
56
57
58
59
60 periods of the lithium dendrites covered with or without the HVS layer was performed on a
three-dimensional (3D) view by COMSOL Multiphysics 5.3a software. The constructed models
referring to size ratio, shape and distribution of materials were established by SolidWorks 2016
according to the experimental characterization results, to make the simulation process as close as
possible to the actual situation. To simplify the module process, the physics module of “Electric
Current Field” under steady-state conditions was used in the subsequent simulation. The
simulated electric field intensity was set to be near platform voltage of 2 V with the direction
from the separator to the anode. The relative dielectric constant of VS₂ was set to 3.1, and the
conductivity of VS₂ was 500 S m⁻¹.⁷¹ The physical field-controlled grids were selected to be the
sequence type and extremely refined cell size.

ASSOCIATED CONTENT

Supporting Information

1
2
3 The Supporting Information is available free of charge on the ACS Publications website at
4 DOI: Figures S1 and S2 show the synthetic route and growth mechanism for the HVS.
5
6 Figures S3-21 show the material characterizations (SEM, TEM, XRD, XPS, AFM and ICP-
7
8 AES), optical images, electrochemical characterizations, calculations and simulations for
9
10 various samples. Tables S1-4 show some calculated electrochemical performance parameters for
11
12 various separators in Li-S batteries, including the lithium-ion diffusion rate, EIS resistance, N/P
13
14 ratio, areal capacity and areal weight.
15
16
17
18
19

20 **Financial Interest Statements**

21
22 The authors declare no conflict of financial interest.
23
24

25 **AUTHOR INFORMATION**

26 **Corresponding Author**

27
28 *E-mail: dingsj@xjtu.edu.cn (S. Ding).
29
30

31
32 *E-mail: yanwei@xjtu.edu.cn (W. Yan).
33
34

35
36 *E-mail: kx210@cam.ac.uk (K. Xi)
37

38 **Author Contributions**

39 J. Wang, K. Xi, W. Yan and S. Ding conceived and designed the work; J. Wang, S. Yi, J.
40 Liu, S. Sun, Y. Liu, D. Yang and G. Gao performed the experiments, characterizations,
41 calculations and simulations; J. Wang and K. Xi wrote the manuscript; J. Wang, K. Xi, A.
42 Abdelkader, W. Yan, S. Ding and R. V. Kumar analyzed the data and revised the
43 manuscript. All authors have given approval to the final version of the manuscript.
44
45
46
47
48
49

50 **ACKNOWLEDGMENTS**

51
52 This work was supported by the Natural Science Foundation of China (No. 51803164;
53
54 51773165), China Postdoctoral Science Foundation (2018M643635), Natural Science
55
56
57
58
59
60

1
2
3 Foundation of Shaanxi Province (2019JQ-126) and Young Talent Support Plan of Xi'an
4 Jiaotong University. The authors thank Zijun Ren and Chao Li at Instrument Analysis
5
6 Center of Xi'an Jiaotong University for their assistance with SEM and TEM analysis.
7
8
9

10 REFERENCES

- 11
12 1. Griffith, K. J.; Wiaderek, K. M.; Cibir, G.; Marbella, L. E.; Grey, C. P. Niobium
13 Tungsten Oxides for High-Rate Lithium-Ion Energy Storage. *Nature* **2018**, *559*, 556-563.
- 14
15 2. Cha, E.; Patel, M. D.; Park, J.; Hwang, J.; Prasad, V.; Cho, K.; Choi, W. 2D MoS₂ as an
16 Efficient Protective Layer for Lithium Metal Anodes in High-Performance Li-S Batteries. *Nat.*
17 *Nanotechnol.* **2018**, *13*, 337-344.
- 18
19 3. Zhang, M.; Xiang, L.; Galluzzi, M.; Jiang, C.; Zhang, S.; Li, J.; Tang, Y. Uniform
20 Distribution of Alloying/Dealloying Stress for High Structural Stability of an Al Anode in High-
21 Areal-Density Lithium-Ion Batteries. *Adv. Mater.* **2019**, *31*, 1900826.
- 22
23 4. Pang, Q.; Shyamsunder, A.; Narayanan, B.; Kwok, C. Y.; Curtiss, L. A.; Nazar, L. F.
24 Tuning the Electrolyte Network Structure to Invoke Quasi-Solid State Sulfur Conversion and
25 Suppress Lithium Dendrite Formation in Li-S Batteries. *Nature Energy* **2018**, *3*, 783-791.
- 26
27 5. Chang, J.; Shang, J.; Sun, Y.; Ono, L. K.; Wang, D.; Ma, Z.; Huang, Q.; Chen, D.; Liu,
28 G.; Cui, Y.; Qi, Y.; Zheng, Z. Flexible and Stable High-Energy Lithium-Sulfur Full Batteries
29 with Only 100% Oversized Lithium. *Nat. Commun.* **2018**, *9*, 4480.
- 30
31 6. Tsao, Y.; Lee, M.; Miller, E. C.; Gao, G.; Park, J.; Chen, S.; Katsumata, T.; Tran, H.;
32 Wang, L.-W.; Toney, M. F.; Cui, Y.; Bao, Z. Designing a Quinone-Based Redox Mediator to
33 Facilitate Li₂S Oxidation in Li-S Batteries. *Joule* **2019**, *3*, 872-884.
- 34
35 7. Wang, J.; Yang, G.; Chen, J.; Liu, Y.; Wang, Y.; Lao, C. Y.; Xi, K.; Yang, D.; Harris, C.
36 J.; Yan, W.; Ding, S.; Kumar, R. V. Flexible and High-Loading Lithium-Sulfur Batteries
37 Enabled by Integrated Three-In-One Fibrous Membranes. *Adv. Energy Mater.* **2019**, *9*, 1902001.
- 38
39 8. Xu, G.; Kushima, A.; Yuan, J.; Dou, H.; Xue, W.; Zhang, X.; Yan, X.; Li, J. Ad Hoc
40 Solid Electrolyte on Acidized Carbon Nanotube Paper Improves Cycle Life of Lithium-Sulfur
41 Batteries. *Energy Environ. Sci.* **2017**, *10*, 2544-2551.
- 42
43
44
45
46
47
48
49
50
51
52
53
54
55
56
57
58
59
60

- 1
2
3 9. Xi, K.; He, D.; Harris, C.; Wang, Y.; Lai, C.; Li, H.; Coxon, P. R.; Ding, S.; Wang, C.;
4 Kumar, R. V. Enhanced Sulfur Transformation by Multifunctional FeS₂/FeS/S Composites for
5 High-Volumetric Capacity Cathodes in Lithium-Sulfur Batteries. *Adv. Sci.* **2019**, *6*, 1800815.
6
7
- 8 10. Lin, D.; Liu, Y.; Cui, Y. Reviving the Lithium Metal Anode for High-Energy Batteries.
9 *Nat. Nanotechnol.* **2017**, *12*, 194-206.
10
- 11 11. Cheng, X. B.; Zhang, R.; Zhao, C. Z.; Zhang, Q. Toward Safe Lithium Metal Anode in
12 Rechargeable Batteries: A Review. *Chem. Rev.* **2017**, *117*, 10403-10473.
13
- 14 12. Lin, H.; Yang, L.; Jiang, X.; Li, G.; Zhang, T.; Yao, Q.; Zheng, G. W.; Lee, J. Y.
15 Electrocatalysis of Polysulfide Conversion by Sulfur-Deficient MoS₂ Nanoflakes for Lithium-
16 Sulfur Batteries. *Energy Environ. Sci.* **2017**, *10*, 1476-1486.
17
- 18 13. Xi, K.; Chen, B.; Li, H.; Xie, R.; Gao, C.; Zhang, C.; Kumar, R. V.; Robertson, J. Soluble
19 Polysulphide Sorption Using Carbon Nanotube Forest for Enhancing Cycle Performance in a
20 Lithium-Sulphur Battery. *Nano Energy* **2015**, *12*, 538-546.
21
- 22 14. Gu, X.; Wang, Y.; Lai, C.; Qiu, J.; Li, S.; Hou, Y.; Martens, W.; Mahmood, N.; Zhang, S.
23 Microporous Bamboo Biochar for Lithium-Sulfur Batteries. *Nano Res.* **2014**, *8*, 129-139.
24
- 25 15. Chen, H.; Ling, M.; Hencz, L.; Ling, H. Y.; Li, G.; Lin, Z.; Liu, G.; Zhang, S. Exploring
26 Chemical, Mechanical, and Electrical Functionalities of Binders for Advanced Energy-Storage
27 Devices. *Chem. Rev.* **2018**, *118*, 8936-8982.
28
- 29 16. He, J.; Chen, Y.; Manthiram, A. Vertical Co₉S₈ Hollow Nanowall Arrays Grown on a
30 Celgard Separator as a Multifunctional Polysulfide Barrier for High-Performance Li-S Batteries.
31 *Energy Environ. Sci.* **2018**, *11*, 2560-2568.
32
- 33 17. Li, G.; Wang, C.; Cai, W.; Lin, Z.; Li, Z.; Zhang, S. The Dual Actions of Modified
34 Polybenzimidazole in Taming the Polysulfide Shuttle for Long-Life Lithium-Sulfur Batteries.
35 *NPG Asia Mater.* **2016**, *8*, e317-e317.
36
- 37 18. Liu, S.; Xia, X.; Zhong, Y.; Deng, S.; Yao, Z.; Zhang, L.; Cheng, X.-B.; Wang, X.;
38 Zhang, Q.; Tu, J. 3D TiC/C Core/Shell Nanowire Skeleton for Dendrite-Free and Long-Life
39 Lithium Metal Anode. *Adv. Energy Mater.* **2018**, *8*, 1702322.
40
- 41 19. Dong, J.; Dai, H.; Fan, Q.; Lai, C.; Zhang, S. Grain Refining Mechanisms: Initial
42 Levelling Stage During Nucleation for High-Stability Lithium Anodes. *Nano Energy* **2019**, *66*,
43 104128.
44
45
46
47
48
49
50
51
52
53
54
55
56
57
58
59
60

- 1
2
3 20. Peng, H.-J.; Huang, J.-Q.; Cheng, X.-B.; Zhang, Q. Review on High-Loading and High-
4 Energy Lithium-Sulfur Batteries. *Adv. Energy Mater.* **2017**, *7*, 1700260.
5
6 21. Bai, S.; Liu, X.; Zhu, K.; Wu, S.; Zhou, H. Metal-Organic Framework-Based Separator
7 for Lithium-Sulfur Batteries. *Nature Energy* **2016**, *1*, 16094.
8
9 22. Lee, Y.-H.; Kim, J.-H.; Kim, J.-H.; Yoo, J.-T.; Lee, S.-Y. Spiderweb-Mimicking Anion-
10 Exchanging Separators for Li-S Batteries. *Adv. Funct. Mater.* **2018**, *28*, 1801422.
11
12 23. Chang, Z.; Qiao, Y.; Wang, J.; Deng, H.; He, P.; Zhou, H. Fabricating Better Metal-
13 Organic Frameworks Separators for Li-S Batteries: Pore Sizes Effects Inspired Channel
14 Modification Strategy. *Energy Storage Mater.* **2020**, *25*, 164-171.
15
16 24. Wu, J.; Zeng, H.; Li, X.; Xiang, X.; Liao, Y.; Xue, Z.; Ye, Y.; Xie, X. Ultralight
17 Layer-By-Layer Self-Assembled MoS₂-Polymer Modified Separator for Simultaneously
18 Trapping Polysulfides and Suppressing Lithium Dendrites. *Adv. Energy Mater.* **2018**, *8*,
19 1802430.
20
21 25. He, Y.; Chang, Z.; Wu, S.; Qiao, Y.; Bai, S.; Jiang, K.; He, P.; Zhou, H. Simultaneously
22 Inhibiting Lithium Dendrites Growth and Polysulfides Shuttle by a Flexible MOF-Based
23 Membrane in Li-S Batteries. *Adv. Energy Mater.* **2018**, *8*, 1802130.
24
25 26. Li, Y. J.; Wang, C.; Wang, W. Y.; Eng, A. Y. S.; Wan, M. T.; Fu, L.; Mao, E. Y.; Li, G.
26 C.; Tang, J.; Seh, Z. W.; Sun, Y. M. Enhanced Chemical Immobilization and Catalytic
27 Conversion of Polysulfide Intermediates Using Metallic Mo Nanoclusters for High-Performance
28 Li-S Batteries. *ACS Nano* **2020**, *14*, 1148-1157.
29
30 27. Li, M.; Wan, Y.; Huang, J.-K.; Assen, A. H.; Hsiung, C.-E.; Jiang, H.; Han, Y.;
31 Eddaoudi, M.; Lai, Z.; Ming, J.; Li, L.-J. Metal-Organic Framework-Based Separators for
32 Enhancing Li-S Battery Stability: Mechanism of Mitigating Polysulfide Diffusion. *ACS Energy*
33 *Lett.* **2017**, *2*, 2362-2367.
34
35 28. Kim, J.-H.; Lee, Y.-H.; Cho, S.-J.; Gwon, J.-G.; Cho, H.-J.; Jang, M.; Lee, S.-Y.; Lee, S.-
36 Y. Nanomat Li-S Batteries Based on All-Fibrous Cathode/Separator Assemblies and Reinforced
37 Li Metal Anodes: Towards Ultrahigh Energy Density and Flexibility. *Energy Environ. Sci.* **2019**,
38 *12*, 177-186.
39
40 29. Pan, Y.; Chou, S.; Liu, H. K.; Dou, S. X. Functional Membrane Separators for Next-
41 Generation High-Energy Rechargeable Batteries. *Natl. Sci. Rev.* **2017**, *4*, 917-933.
42
43
44
45
46
47
48
49
50
51
52
53
54
55
56
57
58
59
60

- 1
2
3 30. Zhou, G.; Tian, H.; Jin, Y.; Tao, X.; Liu, B.; Zhang, R.; Seh, Z. W.; Zhuo, D.; Liu, Y.;
4 Sun, J.; Zhao, J.; Zu, C.; Wu, D. S.; Zhang, Q.; Cui, Y. Catalytic Oxidation of Li₂S on the
5 Surface of Metal Sulfides for Li-S Batteries. *P. Natl. Acad. Sci.* **2017**, *114*, 840-845.
6
7
8 31. Chen, X.; Peng, H.-J.; Zhang, R.; Hou, T.-Z.; Huang, J.-Q.; Li, B.; Zhang, Q. An
9 Analogous Periodic Law for Strong Anchoring of Polysulfides on Polar Hosts in Lithium Sulfur
10 Batteries: S- or Li-Binding on First-Row Transition-Metal Sulfides? *ACS Energy Lett.* **2017**, *2*,
11 795-801.
12
13
14 32. Sun, R.; Wei, Q.; Sheng, J.; Shi, C.; An, Q.; Liu, S.; Mai, L. Novel Layer-By-Layer
15 Stacked VS₂ Nanosheets with Intercalation Pseudocapacitance for High-Rate Sodium Ion Charge
16 Storage. *Nano Energy* **2017**, *35*, 396-404.
17
18
19 33. Yan, J.; Liu, F.; Hu, Z.; Gao, J.; Zhou, W.; Huo, H.; Zhou, J.; Li, L. Realizing Dendrite-
20 Free Lithium Deposition with a Composite Separator. *Nano Lett.* **2020**, *20*, 3798-3807.
21
22
23 34. Fu, C.; Venturi, V.; Kim, J.; Ahmad, Z.; Ells, A. W.; Viswanathan, V.; Helms, B. A.
24 Universal Chemomechanical Design Rules for Solid-Ion Conductors to Prevent Dendrite
25 Formation in Lithium Metal Batteries. *Nat. Mater.* **2020**, DOI: 10.1038/s41563-020-0655-2.
26
27
28 35. Sun, J.; Sun, Y.; Pasta, M.; Zhou, G.; Li, Y.; Liu, W.; Xiong, F.; Cui, Y. Entrapment of
29 Polysulfides by a Black-Phosphorus-Modified Separator for Lithium-Sulfur Batteries. *Adv.*
30 *Mater.* **2016**, *28*, 9797-9803.
31
32
33 36. Ye, H.; Zheng, Z. J.; Yao, H. R.; Liu, S. C.; Zuo, T. T.; Wu, X. W.; Yin, Y. X.; Li, N.
34 W.; Gu, J. J.; Cao, F. F.; Guo, Y. G. Guiding Uniform Li Plating/Stripping through Lithium-
35 Aluminum Alloying Medium for Long-Life Li Metal Batteries. *Angew. Chem. Int. Ed.* **2019**, *58*,
36 1094-1099.
37
38
39 37. Oh, J.; Jo, H.; Lee, H.; Kim, H.-T.; Lee, Y. M.; Ryou, M.-H. Polydopamine-Treated
40 Three-Dimensional Carbon Fiber-Coated Separator for Achieving High-Performance Lithium
41 Metal Batteries. *J. Power Sources* **2019**, *430*, 130-136.
42
43
44 38. Zhang, R.; Cheng, X. B.; Zhao, C. Z.; Peng, H. J.; Shi, J. L.; Huang, J. Q.; Wang, J.; Wei,
45 F.; Zhang, Q. Conductive Nanostructured Scaffolds Render Low Local Current Density to
46 Inhibit Lithium Dendrite Growth. *Adv. Mater.* **2016**, *28*, 2155-2162.
47
48
49
50
51
52
53
54
55
56
57
58
59
60

- 1
2
3 39. Luo, J.; Wang, C.; Wang, H.; Hu, X.; Matios, E.; Lu, X.; Zhang, W.; Tao, X.; Li, W.
4 Pillared Mxene with Ultralarge Interlayer Spacing as a Stable Matrix for High Performance
5 Sodium Metal Anodes. *Adv. Funct. Mater.* **2019**, *29*, 1805946.
6
7
8 40. Koczkur, K. M.; Mourdikoudis, S.; Polavarapu, L.; Skrabalak, S. E. Polyvinylpyrrolidone
9 (PVP) in Nanoparticle Synthesis. *Dalton Trans.* **2015**, *44*, 17883-17905.
10
11 41. Fang, Z.; Hao, S.; Long, L.; Fang, H.; Qiang, T.; Song, Y. The Enhanced
12 Photoelectrochemical Response of SnSe₂ Nanosheets. *CrystEngComm* **2014**, *16*, 2404.
13
14 42. Chen, J. S.; Liu, J.; Qiao, S. Z.; Xu, R.; Lou, X. W. Formation of Large 2D Nanosheets
15 via PVP-Assisted Assembly of Anatase TiO₂ Nanomosaics. *Chem. Commun.* **2011**, *47*, 10443-
16 10445.
17
18 43. Lai, C.; Wu, Z.; Gu, X.; Wang, C.; Xi, K.; Kumar, R. V.; Zhang, S. Reinforced
19 Conductive Confinement of Sulfur for Robust and High-Performance Lithium-Sulfur Batteries.
20 *ACS Appl. Mater. Interfaces* **2015**, *7*, 23885-23892.
21
22 44. Shao, H.; Ai, F.; Wang, W.; Zhang, H.; Wang, A.; Feng, W.; Huang, Y. Crab Shell-
23 Derived Nitrogen-Doped Micro-/Mesoporous Carbon as an Effective Separator Coating for High
24 Energy Lithium-Sulfur Batteries. *J. Mater. Chem. A* **2017**, *5*, 19892-19900.
25
26 45. Ling, Z.; Ren, C. E.; Zhao, M. Q.; Yang, J.; Giammarco, J. M.; Qiu, J.; Barsoum, M. W.;
27 Gogotsi, Y. Flexible and Conductive Mxene Films and Nanocomposites with High Capacitance.
28 *P. Natl. Acad. Sci.* **2014**, *111*, 16676-16681.
29
30 46. Ghazi, Z. A.; He, X.; Khattak, A. M.; Khan, N. A.; Liang, B.; Iqbal, A.; Wang, J.; Sin,
31 H.; Li, L.; Tang, Z. MoS₂/Celgard Separator as Efficient Polysulfide Barrier for Long-Life
32 Lithium-Sulfur Batteries. *Adv. Mater.* **2017**, *29*, 1606817.
33
34 47. Zhang, D.; Wang, S.; Li, B.; Gong, Y.; Yang, S. Horizontal Growth of Lithium on
35 Parallely Aligned Mxene Layers towards Dendrite-Free Metallic Lithium Anodes. *Adv. Mater.*
36 **2019**, *31*, 1901820.
37
38 48. Chen, L.; Li, W.; Fan, L. Z.; Nan, C. W.; Zhang, Q. Intercalated Electrolyte with High
39 Transference Number for Dendrite-Free Solid-State Lithium Batteries. *Adv. Funct. Mater.* **2019**,
40 *29*, 1901047.
41
42 49. Wang, Z.; Huang, W.; Hua, J.; Wang, Y.; Yi, H.; Zhao, W.; Zhao, Q.; Jia, H.; Fei, B.;
43 Pan, F. An Anionic-MOF-Based Bifunctional Separator for Regulating Lithium Deposition and
44
45
46
47
48
49
50
51
52
53
54
55
56
57
58
59
60

1
2
3 Suppressing Polysulfides Shuttle in Li-S Batteries. *Small Methods* **2020**, DOI:
4 10.1002/smt.202000082, 2000082.

5
6 50. Wang, Y.; Zhang, R.; Chen, J.; Wu, H.; Lu, S.; Wang, K.; Li, H.; Harris, C. J.; Xi, K.;
7 Kumar, R. V.; Ding, S. Enhancing Catalytic Activity of Titanium Oxide in Lithium-Sulfur
8 Batteries by Band Engineering. *Adv. Energy Mater.* **2019**, *9*, 1900953.

9
10 51. Yu, M.; Wang, Z.; Wang, Y.; Dong, Y.; Qiu, J. Freestanding Flexible Li₂S Paper
11 Electrode with High Mass and Capacity Loading for High-Energy Li-S Batteries. *Adv. Energy*
12 *Mater.* **2017**, *7*, 1700018.

13
14 52. Cherian, C. T.; Sundaramurthy, J.; Reddy, M. V.; Suresh Kumar, P.; Mani, K.; Pliszka,
15 D.; Sow, C. H.; Ramakrishna, S.; Chowdari, B. V. Morphologically Robust NiFe₂O₄ Nanofibers
16 as High Capacity Li-Ion Battery Anode Material. *ACS Appl. Mater. Interfaces* **2013**, *5*, 9957.

17
18 53. Sun, L.; Wang, D.; Luo, Y.; Wang, K.; Kong, W.; Wu, Y.; Zhang, L.; Jiang, K.; Li, Q.;
19 Zhang, Y.; Wang, J.; Fan, S. Sulfur Embedded in a Mesoporous Carbon Nanotube Network as
20 a Binder-Free Electrode for High-Performance Lithium-Sulfur Batteries. *ACS Nano* **2016**, *10*,
21 1300-1308.

22
23 54. Wang, H.; Zhang, W.; Liu, H.; Guo, Z. A Strategy for Configuration of an Integrated
24 Flexible Sulfur Cathode for High-Performance Lithium-Sulfur Batteries. *Angew. Chem. Int. Ed.*
25 **2016**, *55*, 3992-3996.

26
27 55. Wang, J.; Yang, G.; Wang, L.; Yan, W. Synthesis of One-Dimensional NiFe₂O₄
28 Nanostructures: Tunable Morphology and High-Performance Anode Materials for Li Ion
29 Batteries. *J. Mater. Chem. A* **2016**, *4*, 8620-8629.

30
31 56. Mao, Y.; Li, G.; Guo, Y.; Li, Z.; Liang, C.; Peng, X.; Lin, Z. Foldable Interpenetrated
32 Metal-Organic Frameworks/Carbon Nanotubes Thin Film for Lithium-Sulfur Batteries. *Nat.*
33 *Commun.* **2017**, *8*, 14628.

34
35 57. Wang, L.; He, Y.-B.; Shen, L.; Lei, D.; Ma, J.; Ye, H.; Shi, K.; Li, B.; Kang, F. Ultra-
36 Small Self-Discharge and Stable Lithium-Sulfur Batteries Achieved by Synergetic Effects of
37 Multicomponent Sandwich-Type Composite Interlayer. *Nano Energy* **2018**, *50*, 367-375.

38
39 58. Zhang, R.; Li, N. W.; Cheng, X. B.; Yin, Y. X.; Zhang, Q.; Guo, Y. G. Advanced
40 Micro/Nanostructures for Lithium Metal Anodes. *Adv. Sci.* **2017**, *4*, 1600445.

- 1
2
3 59. Liu, B.; Zhang, Y.; Pan, G.; Ai, C.; Deng, S.; Liu, S.; Liu, Q.; Wang, X.; Xia, X.; Tu, J.
4 Ordered Lithiophilic Sites to Regulate Li Plating/Stripping Behavior for Superior Lithium Metal
5 Anodes. *J. Mater. Chem. A* **2019**, *7*, 21794-21801.
6
7
8 60. Cheng, X.-B.; Peng, H.-J.; Huang, J.-Q.; Zhang, R.; Zhao, C.-Z.; Zhang, Q. Dual-Phase
9 Lithium Metal Anode Containing a Polysulfide-Induced Solid Electrolyte Interphase and
10 Nanostructured Graphene Framework for Lithium-Sulfur Batteries. *ACS Nano* **2015**, *9*, 6373-
11 6382.
12
13
14
15 61. Wang, A.; Deng, Q.; Deng, L.; Guan, X.; Luo, J. Eliminating Tip Dendrite Growth by
16 Lorentz Force for Stable Lithium Metal Anodes. *Adv. Funct. Mater.* **2019**, *29*, 1902630.
17
18
19 62. Abe, Y.; Kumagai, S. Effect of Negative/Positive Capacity Ratio on the Rate and Cycling
20 Performances of LiFePO₄/Graphite Lithium-Ion Batteries. *J. Energy Storage* **2018**, *19*, 96-102.
21
22 63. Lu, K.; Liu, Y.; Chen, J.; Zhang, Z.; Cheng, Y. Redox Catalytic and Quasi-Solid Sulfur
23 Conversion for High-Capacity Lean Lithium Sulfur Batteries. *ACS Nano* **2019**, *13*, 14540-14548.
24
25 64. Wu, H.; Huan, Y.; Wang, D.; Li, M.; Cheng, X.; Bai, Z.; Wu, P.; Peng, W.; Zhang, R.; Ji,
26 Z.; Zou, M.; Yan, X. Hierarchical VS₂ Nano-Flowers as Sulfur Host for Lithium Sulfur Battery
27 Cathodes. *J. Electrochem. Soc.* **2019**, *166*, A188-A194.
28
29
30
31 65. Cheng, Z.; Xiao, Z.; Pan, H.; Wang, S.; Wang, R. Elastic Sandwich-Type RGO-VS₂/S
32 Composites with High Tap Density: Structural and Chemical Cooperativity Enabling Lithium-
33 Sulfur Batteries with High Energy Density. *Adv. Energy Mater.* **2018**, *8*, 1702337.
34
35
36 66. Guo, Y.; Zhang, Y.; Zhang, Y.; Xiang, M.; Wu, H.; Liu, H.; Dou, S. Interwoven V₂O₅
37 Nanowire/Graphene Nanoscroll Hybrid Assembled as Efficient Polysulfide-Trapping-
38 Conversion Interlayer for Long-Life Lithium-Sulfur Batteries. *J. Mater. Chem. A* **2018**, *6*,
39 19358-19370.
40
41
42
43 67. Dong, Y.; Zheng, S.; Qin, J.; Zhao, X.; Shi, H.; Wang, X.; Chen, J.; Wu, Z. S. All-
44 Mxene-Based Integrated Electrode Constructed by Ti₃C₂ Nanoribbon Framework Host and
45 Nanosheet Interlayer for High-Energy-Density Li-S Batteries. *ACS Nano* **2018**, *12*, 2381-2388.
46
47
48 68. Feng, J.; Sun, X.; Wu, C.; Peng, L.; Lin, C.; Hu, S.; Yang, J.; Xie, Y. Metallic Few-
49 Layered VS₂ Ultrathin Nanosheets: High Two-Dimensional Conductivity for In-Plane
50 Supercapacitors. *J. Am. Chem. Soc.* **2011**, *133*, 17832-17838.
51
52
53 69. Kresse, G.; Furthmüller, J. Efficient Iterative Schemes for *Ab Initio* Total-Energy
54 Calculations Using a Plane-Wave Basis Set. *Phys. Rev. B* **1996**, *54*, 11169-11186.
55
56
57
58
59
60

- 1
2
3 70. Kresse, G.; Hafner, J. *Ab Initio* Molecular-Dynamics Simulation of the Liquid-Metal-
4 Amorphous-Semiconductor Transition in Germanium. *Phys. Rev. B* **1994**, *49*, 14251-14269.
5
6 71. Yu, D.; Pang, Q.; Gao, Y.; Wei, Y.; Wang, C.; Chen, G.; Du, F. Hierarchical Flower-Like
7 VS₂ Nanosheets-a High Rate-Capacity and Stable Anode Material for Sodium-Ion Battery.
8 *Energy Storage Mater.* **2018**, *11*, 1-7.
9
10
11
12
13
14
15
16
17
18
19
20
21
22
23
24
25
26
27
28
29
30
31
32
33
34
35
36
37
38
39
40
41
42
43
44
45
46
47
48
49
50
51
52
53
54
55
56
57
58
59
60

1
2
3 **For Table of Contents Use Only**
4

5 **Suppressing the Shuttle Effect and Dendrite Growth in Lithium-Sulfur Batteries**
6

